ARTICLES
https://doi.org/10.1038/s41565-021-00848-w
nature nanotechnology

Check for updates

Layer-by-layer anionic diffusion in two-dimensional halide perovskite vertical heterostructures

Akriti[1,7], Enzheng Shi[1,2,7], Stephen B. Shiring[1,7], Jiaqi Yang[3], Cindy L. Atencio-Martinez[1,6], Biao Yuan[4], Xiangchen Hu[4], Yao Gao[1], Blake P. Finkenauer[1], Alan J. Pistone[1], Yi Yu[4], Peilin Liao[3], Brett M. Savoie[1] and Letian Dou[1,5] ✉

Anionic diffusion in a soft crystal lattice of hybrid halide perovskites affects their stability, optoelectronic properties and the resulting device performance. The use of two-dimensional (2D) halide perovskites improves the chemical stability of perovskites and suppresses the intrinsic anionic diffusion in solid-state devices. Based on this strategy, devices with an enhanced stability and reduced hysteresis have been achieved. However, a fundamental understanding of the role of organic cations in inhibiting anionic diffusion across the perovskite–ligand interface is missing. Here we demonstrate the first quantitative investigation of the anionic interdiffusion across atomically flat 2D vertical heterojunctions. Interestingly, the halide diffusion does not follow the classical diffusion process. Instead, a 'quantized' layer-by-layer diffusion model is proposed to describe the behaviour of the anionic migration in 2D halide perovskites. Our results provide important insights into the mechanism of anionic diffusion in 2D perovskites and provide a new materials platform with an enhanced stability for heterostructure integration.

Halide perovskites are promising semiconductors for next-generation solution-processed optoelectronics, but their remarkable properties are often overshadowed by their poor material stability[1–7]. The intrinsic instability of perovskites is dictated by the 'soft' ionic framework. This soft lattice enables a high ionic mobility, which results in detrimental impacts on perovskite-based optoelectronic devices, such as current–voltage hysteresis, spontaneous phase segregation in alloys, diminished transistor behaviour at room temperature and photoinduced self-poling effects[8–12]. Recently, direct visualization of ion migration in three-dimensional (3D) perovskite heterostructures was realized and the solid-state diffusivity of halides is estimated to be in the order of 10^{-14} to 10^{-18} $m^2 s^{-1}$ at a temperature slightly above room temperature, which is dramatically higher than that of Si or oxide perovskites[13–16].

To address the intrinsic stability issue, 2D halide perovskites that incorporate hydrophobic organic capping ligands have been studied as promising alternatives[17–19]. In the past few years, high-performance optoelectronics with an improved stability and suppressed anion migration were demonstrated using polycrystalline quasi-2D perovskite thin films[20–22]. However, a comprehensive quantitative analysis of the factors that impact anionic migration in these 2D halide perovskites is still lacking. This is largely limited by the difficulty of obtaining a clean system free from uncertain variables, such as defects, grain boundaries and phase impurities. Here we demonstrate the first quantitative investigation of the anionic interdiffusion across atomically flat 2D perovskite vertical heterojunctions. Interestingly, the halide diffusion does not follow the classical process. Instead, a 'quantized' layer-by-layer diffusion model is proposed to describe the behaviour of the anionic migration in 2D perovskites. These results provide important insights into the mechanism of anionic diffusion in 2D perovskites and provide a new materials platform for heterostructure construction and device integration.

Assembly of vertical heterostructures

The vertical heterostructures are assembled by transferring the bulk crystals of the top iodide layer onto the pregrown bromide nanocrystals[23] using mechanical exfoliation (Fig. 1a and Supplementary Fig. 1). Independently synthesizing the perovskite layers before assembling the heterostructure ensures a higher phase purity compared with those of previously reported techniques of heterostructure construction using sequential growth[24] or chemical vapour deposition[25–27]. Following this synthesis strategy, we constructed a variety of high-quality bromide–iodide 2D perovskite vertical heterostructures.

We first assembled a $(BA)_2PbBr_4$–$(BA)_2(MA)_2Pb_3I_{10}$ vertical heterostructure (BA, butylammonium cation; MA, methylammonium cation). Figure 1b shows the atomic force microscopy (AFM) image of a representative vertical heterostructure with a total thickness of ~6.4 nm. A scanning electron microscopy (SEM) image and the corresponding energy-dispersive X-ray spectroscopy (EDS) elemental mappings of lead, bromine and iodine for the $(BA)_2PbBr_4$–$(BA)_2(MA)_2Pb_3I_{10}$ vertical heterostructure are shown in Fig. 1c–f. The spatial confinement of the photoluminescence (PL) emission was captured using confocal PL laser scanning microscopy (Fig. 1g–i). Interestingly, confocal PL mapping indicates that the blue emission (the 410–460 nm channel) is limited to the pure bromide region and is largely blocked by the top iodide layer in the junction area due to absorption and/or energy transfer[28–33]. The two peaks in the PL emission spectrum shown in Fig. 1j correspond to the band-edge emissions from the $(BA)_2PbBr_4$ (~410 nm) and the $(BA)_2(MA)_2Pb_3I_{10}$ (~615 nm) layers, respectively. The interface of the reference $(BA)_2PbBr_4$–$(BA)_2(MA)_2Pb_3I_{10}$

[1]Davidson School of Chemical Engineering, Purdue University, West Lafayette, IN, USA. [2]School of Engineering, Westlake University, Hangzhou, China. [3]School of Materials Engineering, Purdue University, West Lafayette, IN, USA. [4]School of Physical Science and Technology, ShanghaiTech University, Shanghai, China. [5]Birck Nanotechnology Center, Purdue University, West Lafayette, IN, USA. [6]Present address: Department of Chemical Engineering, University of Los Andes, Bogotá, Colombia. [7]These authors contributed equally: Akriti, Enzheng Shi, Stephen B. Shiring. ✉e-mail: dou10@purdue.edu

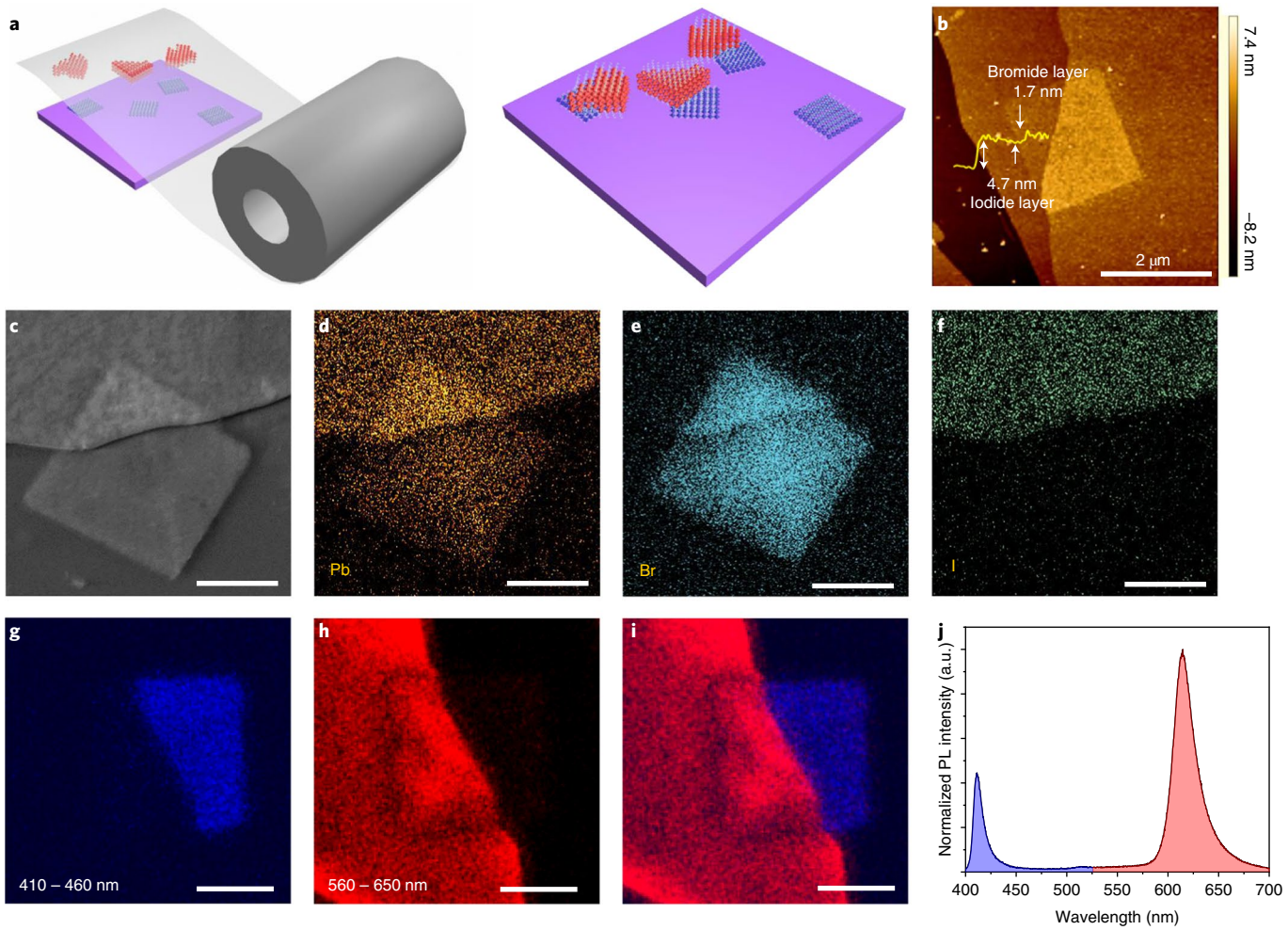

Fig. 1 | Assembly and characterization of $(BA)_2PbBr_4$–$(BA)_2(MA)_2Pb_3I_{10}$ vertical heterostructure. a, Assembly of a bromide–iodide perovskite vertical heterostructure by the mechanical exfoliation of iodide perovskite on bromide perovskite using Scotch tape. **b**, AFM image of a vertical heterostructure with the thicknesses of bromide and iodide layers shown. Scale bar, 2 μm. **c**, SEM image of a representative vertical heterostructure. **d**,**e**,**f**, EDS elemental mappings of Pb, Br and I, respectively, for the SEM image in **c**. Scale bars, 5 μm. **g**,**h**, Confocal PL mappings of the vertical heterostructure using a 405 nm laser as the excitation wavelength and emission channel widths of 410–460 nm and 560–650 nm, respectively. Scale bars, 5 μm. **i**, Dual-channel confocal PL mapping by superimposing **g** and **h**. Scale bar, 5 μm. **j**, PL spectrum of the vertical heterostructure at room temperature depicting blue emission (~410 nm) from the bromide layer and red emission (~615 nm) from the iodide layer. a.u., arbitrary units.

vertical heterostructure is elucidated by the cross-sectional scanning transmission electron microscopy (STEM) and elemental analysis (Extended Data Fig. 1).

Mechanism of halide diffusion

Halide interdiffusion across the vertical heterojunction was monitored during the heating process by tracking the change in PL spectra. PL emission tracking was used for the anionic diffusion study rather than cross-sectional STEM/EDS mapping due to its relative simplicity and non-destructive nature. The bromide–iodide interdiffusion was observed and analysed at different temperatures. Figure 2a,f,k shows the bright-field images of the $(BA)_2PbBr_4$–$(BA)_2(MA)_2Pb_3I_{10}$ vertical heterostructures, and Fig. 2b,g,l shows the corresponding PL images at room temperature. The evolution of the PL emissions after heating at 60, 80 and 100 °C are depicted through PL images and PL spectra in Fig. 2c–e,h–j,m–o, respectively. The emergence of an intermediate green PL emission is an indication of halide diffusion between the top and bottom 2D perovskites of the vertical heterostructure. It is important to note that, irrespective of the temperature and duration of heating, the green PL emission centred at 512–515 nm was observed for all the vertical heterostructures. The appearance of a single alloy PL emission is distinct from the PL evolution profiles reported for halide interdiffusion in 3D perovskites[13–16]. The green alloy PL emission is localized to the junction area, whereas non-overlapping bromide and iodide perovskites maintain their respective intrinsic blue and red PL emissions even after heating. The spatial confinement of the green PL emission is further evidenced by the confocal imaging of the reference $(BA)_2PbBr_4$–$(BA)_2(MA)_2Pb_3I_{10}$ vertical heterostructure at room temperature and after heating for four hours at 80 °C (Supplementary Fig. 2). The localized green emission at the heterojunction area can be attributed to a considerably shorter vertical thickness (nanometre scale) compared with the lateral length (micrometre scale) of the heterostructures. Additionally, the halide alloy PL progressively increased in intensity with an increase in heating time until it reached a steady state of bromide–iodide intermixing.

Additional experiments were conducted to investigate the origin of halide alloy PL emission. In the first experiment, the $(BA)_2PbBr_4$–$(BA)_2(MA)_2Pb_3I_{10}$ vertical heterostructure was heated at 80 °C for a prolonged duration of ~40 hours to facilitate lateral halide interdiffusion into the pristine bromide and iodide layers (Extended Data

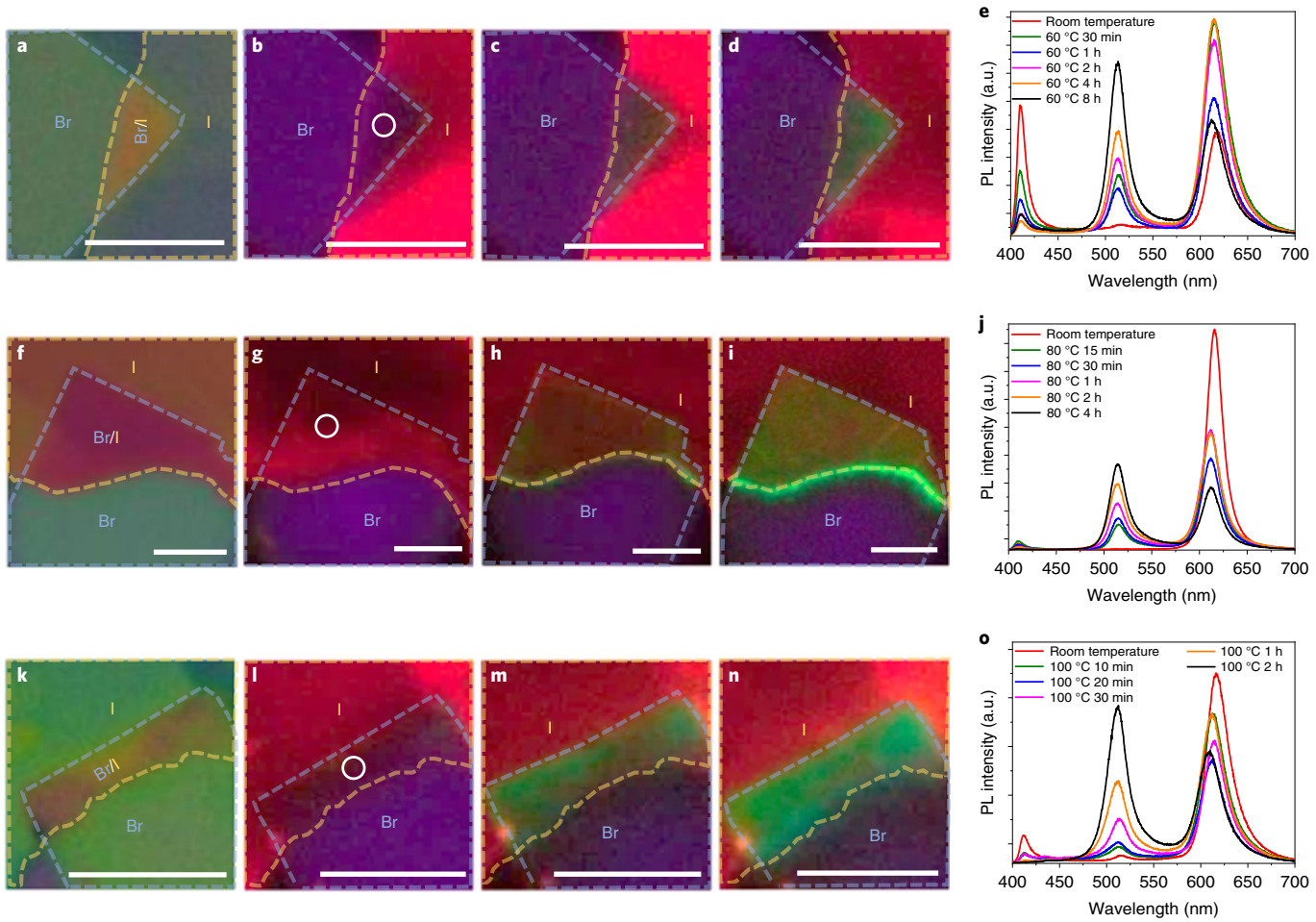

Fig. 2 | Temperature dependence of halide interdiffusion in $(BA)_2PbBr_4$–$(BA)_2(MA)_2Pb_3I_{10}$ vertical heterostructures. a,**f**,**k**, Bright-field images of three independent $(BA)_2PbBr_4$–$(BA)_2(MA)_2Pb_3I_{10}$ vertical heterostructures. **b**,**g**,**l**, Corresponding PL images of the vertical heterostructures at room temperature. The circled regions denote the area used for the PL emission measurement of the heterostructure. **c**,**d**, PL images of the vertical heterostructure in **a** after heating at 60 °C for 1 and 8 h, respectively. **h**,**i**, PL images of the vertical heterostructure in **f** after heating at 80 °C for 1 and 4 h, respectively. **m**,**n**, PL images of the vertical heterostructure in **k** after heating at 100 °C for 1 and 2 h, respectively. Dashed lines are added in all the bright-field and PL images to ease the distinction between the bromide (light blue) and iodide (yellow) domains. Scale bars, 5 μm. **e**,**j**,**o**, Evolution of PL spectra of the three vertical heterostructures upon heating at 60, 80 and 100 °C, respectively. a.u., arbitrary units.

Fig. 2a–d). Interestingly, the green emission extended outside the junction area to the bottom bromide layer, which suggests that the green emission originates from the bottom bromide layer. In the second experiment, a large bulk crystal of iodide perovskite (which could easily be removed later) was placed on top of the pregrown bromide nanocrystals to form the vertical heterostructure. The vertical heterostructure was then heated at 80 °C for four hours, after which the bulk iodide crystal was removed. A strong green PL emission was observed from the bromide layer after removing the iodide bulk crystal (Extended Data Fig. 2e–h). EDS mapping of the bromide crystal clearly showed a dominant iodine composition after heating (Extended Data Fig. 3). An alternate possibility for the green emission is the formation of a new perovskite phase after heating the vertical heterostructure. To exclude this possibility, $(BA)_2PbI_4$–$(BA)_2(MA)_2Pb_3I_{10}$ and $(BA)_2PbBr_4$–$(BA)_2(MA)_2Pb_3Br_{10}$ vertical heterostructures with identical halides in both layers were assembled. No new PL emissions emerged after heating, which indicates that no new perovskite phases were formed (Extended Data Fig. 4a–h). Therefore, based on these control experiments, we conclude that the green emission observed during the thermal diffusion studies originates from the bottom bromide layer after alloy formation.

It is important to highlight that for the same thickness of the top and bottom 2D perovskite layers in the vertical heterostructure, the number of diffusing iodide ions in $(BA)_2(MA)_2Pb_3I_{10}$ ($n=3$) is substantially higher compared with that of bromide ions due to the larger number of organic barriers in the $(BA)_2PbBr_4$ ($n=1$) perovskite. If overall charge neutrality is maintained, the number of halides remain the same before and after the diffusion process. This results in a greater impact of interdiffusion on the average composition of bromide perovskite, and thus potentially leads to the formation of an iodide-dominant $(BA)_2PbBr_{4x}I_{4(1-x)}$ alloy with a green PL emission. The impact of the relative halide concentration was investigated by assembling a $(BA)_2(MA)_2Pb_3Br_{10}$–$(BA)_2PbI_4$ vertical heterostructure, which contrasts our reference case $(BA)_2PbBr_4$–$(BA)_2(MA)_2Pb_3I_{10}$ because, in the new system, each layer of the bottom bromide perovskite ($(BA)_2(MA)_2Pb_3Br_{10}$, $n=3$) has thrice as many bromide ions as iodide ions in each layer of the top iodide perovskite ($(BA)_2PbI_4$, $n=1$) (Extended Data Fig. 4i–l). An orange-red PL emission was observed after heating the $(BA)_2(MA)_2Pb_3Br_{10}$–$(BA)_2PbI_4$ vertical heterostructure at 80 °C, which is characteristic of an iodide-dominant $(BA)_2(MA)Pb_3Br_{10x}I_{10(1-x)}$ perovskite rather than a bromide-dominant $(BA)_2PbBr_{4x}I_{4(1-x)}$ perovskite. Hence, the formation of the iodide-dominant $(BA)_2PbBr_{4x}I_{4(1-x)}$ alloy perovskite

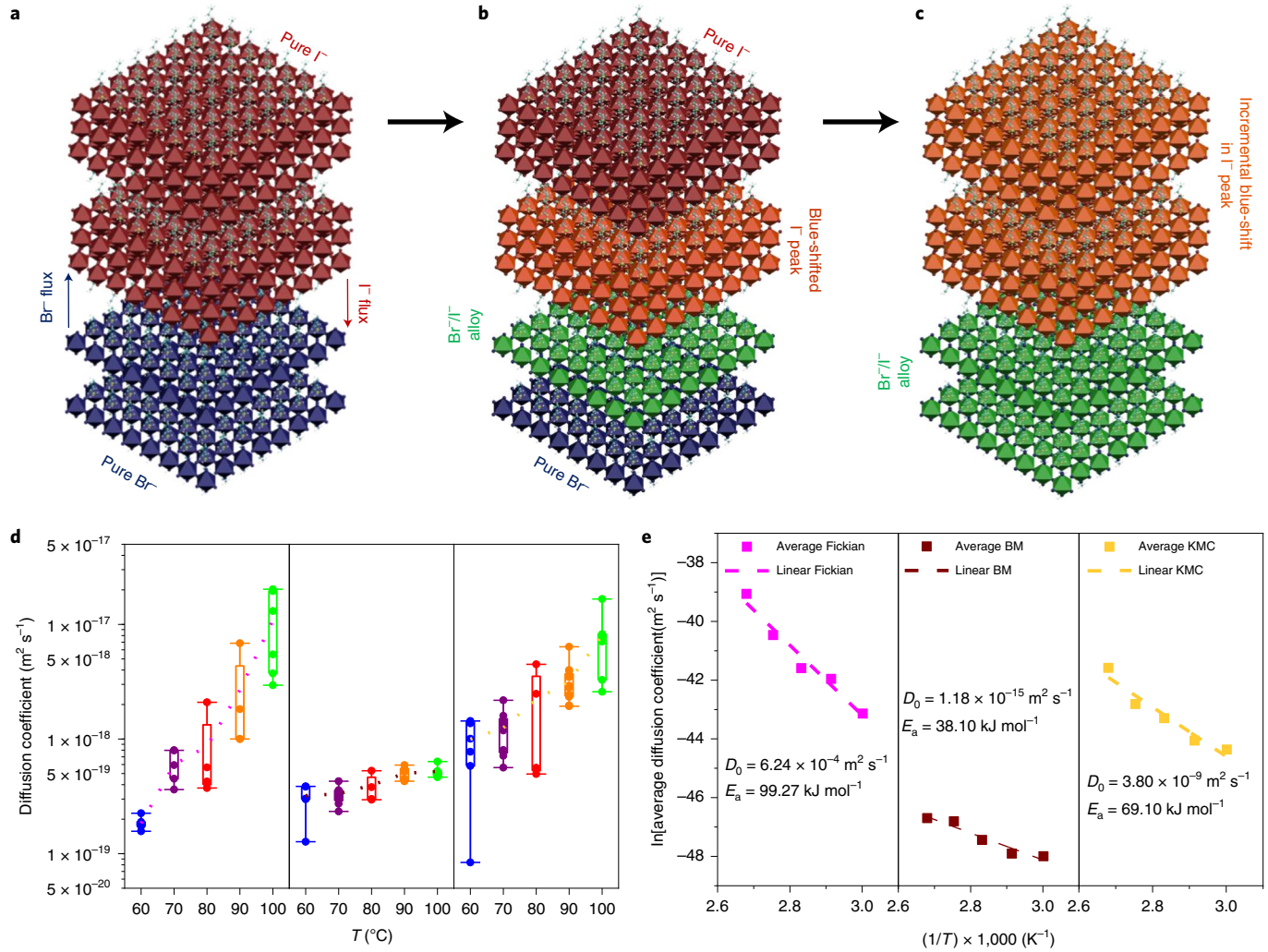

Fig. 3 | Proposed mechanism and calculated diffusion coefficients for halide interdiffusion in 2D perovskite vertical heterostructures. a, Schematic of the vertical heterostructure before heating showing the direction of bromide and iodide diffusion fluxes at the interface. **b**,**c**, Schematics of a vertical heterostructure depicting layer-by-layer halide diffusion during the heating process. The red to orange shift in the iodide layer emission denotes a marginal compositional change in the iodide layer. Similarly, the blue to green shift in the bromide layer symbolizes a substantial compositional change in the bromide layer. **d**, Plot of bromide–iodide interdiffusion coefficients for $(BA)_2PbBr_4$–$(BA)_2(MA)_2Pb_3I_{10}$ vertical heterostructures at five temperature points (T = 60, 70, 80, 90 and 100 °C) for Fickian diffusion coefficients (left), non-Fickian diffusion coefficients calculated using the BM method (middle) and diffusion coefficients obtained using a KMC simulation (right). Boxes represent data points between the 25 and 75 percentiles of the range, the whiskers represent the minimum-to-maximum range and the dashed lines highlight the average diffusion coefficients of the sample data points. **e**, The average halide interdiffusion coefficients (scatter points) calculated using the three methods at five temperatures fitted with an Arrhenius equation (dashed line).

in the reference $(BA)_2PbBr_4$–$(BA)_2(MA)_2Pb_3I_{10}$ vertical heterostructure is not just related to the stoichiometric ratio of diffusing bromide–iodide ions but is also governed by the thermodynamics of the associated alloys[34–36].

Density functional theory (DFT) calculations were performed to understand the impact of halide compositions on the band structures of $(BA)_2PbBr_{4x}I_{4(1-x)}$ and $(BA)_2(MA)Pb_3Br_{10x}I_{10(1-x)}$ perovskites. Projected density of states that highlight the bandgaps for $(BA)_2PbI_4$, $(BA)_2PbBr_4$, $(BA)_2(MA)_2Pb_3I_{10}$ and $(BA)_2(MA)_2Pb_3Br_{10}$ are shown in Supplementary Fig. 3a–d, respectively. The experimentally measured PL energies for a varying bromide mole fractions (x_{Br}) in $(BA)_2PbBr_{4x}I_{4(1-x)}$ perovskites are plotted in Supplementary Fig. 4a. Interestingly, both experimental data and DFT calculations predict negligible changes in the PL emissions and bandgaps for $0 \leq x_{Br} \leq 0.5$. Therefore, once the iodide diffusion into the bottom bromide perovskite layer reaches $x_{Br} = 0.5$, changes in the PL emission become less obvious with additional iodide influx. The DFT-calculated bandgap versus the x_{Br} calibration curve is plotted for $(BA)_2(MA)Pb_3Br_{10x}I_{10(1-x)}$ perovskites in Supplementary Fig. 4b. It can be concluded from the plot that for the top iodide layer, no obvious change in PL energy and composition can be distinguished for $0 \leq x_{Br} \leq 0.3$. From the PL spectra evolution during heating of the $(BA)_2PbBr_4$–$(BA)_2(MA)_2Pb_3I_{10}$ vertical heterostructure, it is evident that the iodide-dominant alloy ($(BA)_2PbBr_{4x}I_{4(1-x)}$ with $x \leq 0.5$) forms in the bottom layer within minutes of heating. Furthermore, the incremental energy required for the substitution of iodine atoms in the $(BA)_2PbBr_4$ perovskite (calculated by DFT) decreases substantially for $x_{Br} \leq 0.4$ (Supplementary Fig. 4c). This result indicates that it is energetically favourable to form iodide-dominant halide alloys in $(BA)_2PbBr_{4x}I_{4(1-x)}$ perovskites once the barrier for the initial energy states is overcome and therefore the diffusion to the next layer is limited by this energy threshold.

The above observations regarding the origin of the green PL emission and formation of the thermodynamically preferred

alloy composition provide important insights into the mechanism of halide interdiffusion across the vertical heterojunction. Supplementary Fig. 5a–c,g provides a schematic illustration of the halide migration and the corresponding concentration-profile evolution during the heating process as predicted by the classic Fickian diffusion model. However, this continuous concentration profile is contrary to the experimental observations of the emergence of a single halide alloy composition. To more precisely depict the experimental observations, a layer-by-layer mechanism is proposed and schematically represented in Fig. 3a–c and Supplementary Fig. 5d–f. This is based on the key findings that a preferential halide alloy composition formed exclusively in the bottom perovskite layer and the heterostructure achieved a steady state when all the bottom perovskite layers attained this preferred composition during the heating process. Meanwhile, the diffusion of bromide into the top layer only led to a small PL shift, as indicated in Fig. 2e,j,o and Supplementary Fig. 4b ($0 \leq x_{Br} \leq 0.3$). The corresponding concentration profile evolution for this proposed quantized model is captured in Supplementary Fig. 5h.

Diffusion coefficient calculations

Owing to the complex absorption and energy transfer processes between perovskite layers, it is challenging to accurately obtain the evolution of the concentration profile during the diffusion process. However, the diffusion coefficient can be estimated based solely on the initial and final equilibrium states. The halide interdiffusion coefficient across vertical heterojunctions was calculated analytically using Fickian and non-Fickian mathematical models and estimated from the kinetic Monte Carlo (KMC) simulations.

The Fickian mathematical model utilizes Fick's second law, which describes a one-dimensional (1D) transient diffusion problem stated as follows[37]:

$$\frac{\partial C}{\partial t} = D\frac{\partial^2 C}{\partial x^2} \tag{1}$$

where C is the concentration of bromide, t is the heating time, x is the diffusion length and D is the halide interdiffusion coefficient. The solution of this ideal 1D diffusion problem is given by:

$$C = \frac{1}{2}C_0 \mathrm{erfc}\frac{x}{2(Dt)^{\frac{1}{2}}} \tag{2}$$

where erfc is the complementary error function and C_0 is the initial bromide concentration in the bottom perovskite[38].

The non-Fickian mathematical model utilizes a concentration-dependent diffusion coefficient, D_C, which describes a 1D transient diffusion problem stated as follows[38]:

$$\frac{\partial C}{\partial t} = \frac{\partial}{\partial x}\left(D(C)\frac{\partial C}{\partial x}\right) \tag{3}$$

The diffusion coefficient is calculated by utilizing the fact that, at equilibrium, all the bottom layers in the vertical heterostructure attain the preferred halide alloy composition as depicted by the curve t_f in Supplementary Fig. 5h. The concentration profile at the final time step is fitted with a Gaussian distribution and the diffusion coefficient is then calculated by the Boltzmann–Matano (BM) method[38,39]:

$$D(c^*) = -\frac{1}{2t}\frac{\int_{c_1}^{c^*}(x - x_M)\mathrm{d}c}{\left(\frac{\mathrm{d}c}{\mathrm{d}x}\right)_{c^*}} \tag{4}$$

where c^* is the bromide mole fraction in the preferred halide alloy, c_1 is the bromide mole fraction in the top perovskite layer and x_M is the Matano interface (a mathematical parameter that divides the concentration profile into two equal-area plots). A representative example of the experimental data used to obtain the equation parameters and calculate the interdiffusion coefficient for the $(BA)_2PbBr_4$–$(BA)_2(MA)_2Pb_3I_{10}$ vertical heterostructure using both Fickian and non-Fickian diffusion models is depicted in Supplementary Fig. 6. Details of the calculation steps involved in converting the experimental observations into mathematical parameters are provided in the Supplementary Information.

Although the non-Fickian diffusion model is based on the final concentration profile across the vertical heterostructure, it does not capture the unique layer-by-layer alloy-mediated diffusion process observed in the 2D vertical heterostructures. To model the impact of the layer-by-layer preferred alloy formation on the interdiffusion coefficient, KMC lattice-diffusion simulations were performed. The simulated lattices consisted of sites that corresponded to Pb octahedra. Layers that represented Br^-- or I^--dominant perovskite sheets were initialized in accordance with the experimental assembly of vertical heterostructures. To capture the experimental behaviour of the heterostructure to equilibrate to a preferred halide alloy composition, as well as to model the proposed layer-by-layer diffusion mechanism, a concentration threshold criterion for the interlayer diffusion was introduced. This concentration threshold criterion suppressed halide diffusion from a given layer into an adjacent layer until the experimentally observed preferred halide alloy concentration was attained in the originating layer. Thus, diffusing ions 'spilled over' one layer to the next in a quantized manner instead of diffusing continuously throughout the heterostructure. The interlayer hopping rates, k, were fitted so that the elapsed simulation time required for the bottom perovskite layer to reach its thermodynamically preferred alloy composition reproduced the experimental time. Once the transition rates were determined, the diffusion coefficients were calculated by $D = kh_{Br}^2$ where h_{Br} is the bromide layer thickness. Further details on the KMC methodology are available in Methods (Simulations).

The calculated diffusion coefficients using Fickian, BM and KMC models at 60, 70, 80, 90 and 100 °C are plotted in Fig. 3d. Additionally, a plot of the average diffusion coefficient using the three mathematical models versus temperature is shown in Fig. 3e. The calculated diffusion coefficients were compared with the theoretical predictions of the Arrhenius equation:

$$D = D_0\exp\left(-\frac{E_a}{RT}\right) \Rightarrow \ln D = \ln D_0 - \frac{E_a}{R}\left(\frac{1}{T}\right) \tag{5}$$

where, D_0 is a constant, E_a is the activation energy for vacancy-assisted halide migration, R is the universal gas constant ($R = 8.314\,\mathrm{J\,(K^{-1}\,mol^{-1})}$) and T is the heating temperature (Fig. 3e)[40,41]. The calculated diffusion coefficients show a good fit to the exponential temperature dependence, which provides additional credibility to the mathematical models used to quantify the halide interdiffusion coefficients.

Impact of inorganic and organic layers on halide diffusion

The halide interdiffusion was analysed for three additional heterostructures constructed by using different inorganic layer thicknesses for the top iodide perovskite. Figure 4 shows the schematic representations (Fig. 4a,d,g), bright-field images (Fig. 4b,e,h) and PL images (Fig. 4c,f,h) of the $(BA)_2PbBr_4$-$(BA)_2PbI_4$, $(BA)_2PbBr_4$-$(BA)_2(MA)Pb_2I_7$ and $(BA)_2PbBr_4$-$(BA)_2(MA)_4Pb_5I_{16}$ vertical heterostructures, respectively. The bromide–iodide diffusion across the vertical heterojunctions was analysed by heating at 80 °C and monitoring the PL (Supplementary Figs. 7–9). It is interesting that the emergence of a single halide alloy PL centred at 508–518 nm was also observed for $(BA)_2PbBr_4$–$(BA)_2(MA)Pb_2I_7$ (Supplementary Fig. 8) and $(BA)_2PbBr_4$–$(BA)_2(MA)_4Pb_5I_{16}$ (Supplementary Fig. 9).

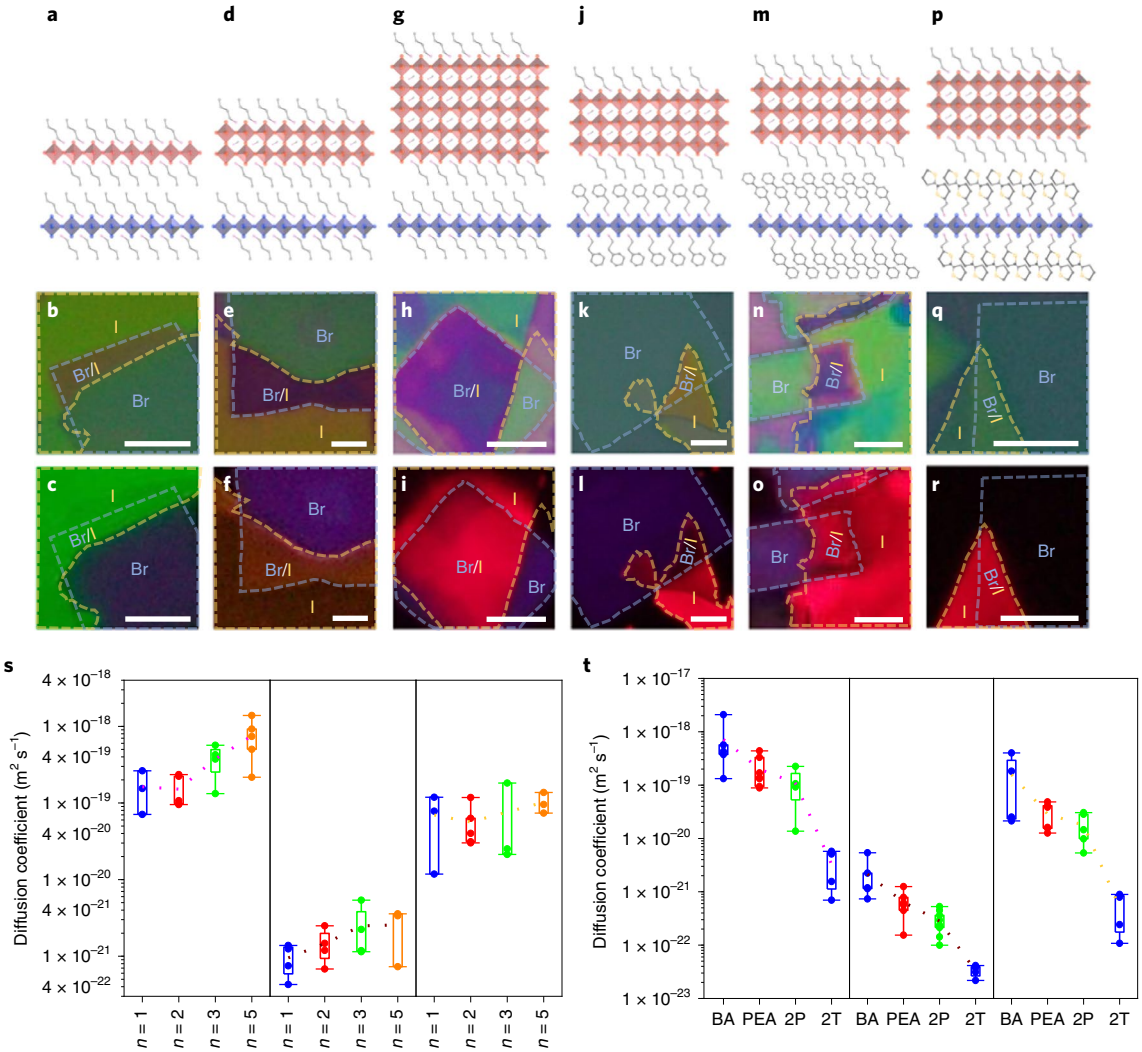

Fig. 4 | Effect of inorganic layer thickness and organic cation on halide diffusion in $(L)_2PbBr_4$–$(BA)_2(MA)_{n-1}Pb_nI_{3n+1}$ (L, organic cation; $n = 1$, 2, 3 or 5) vertical heterostructures. a,**d**,**g**,**j**,**m**,**p**, Schematic representations of $(BA)_2PbBr_4$–$(BA)_2(MA)_{n-1}Pb_nI_{3n+1}$ ($n = 1$, 2 or 5) and $(L)_2PbBr_4$–$(BA)_2(MA)_2Pb_3I_{10}$ (L = PEA, 2P or 2T) vertical heterostructures, respectively. For clarity, no hydrogen atoms are shown in the organic cations. **b**,**e**,**h**,**k**,**n**,**q**, Bright-field images of $(BA)_2PbBr_4$–$(BA)_2(MA)_{n-1}Pb_nI_{3n+1}$ ($n = 1$, 2 or 5) and $(L)_2PbBr_4$–$(BA)_2(MA)_2Pb_3I_{10}$ (L = PEA, 2P or 2T) vertical heterostructures, respectively. **c**,**f**,**i**,**l**,**o**,**r**, PL images of $(BA)_2PbBr_4$–$(BA)_2(MA)_{n-1}Pb_nI_{3n+1}$ ($n = 1$, 2 or 5) and $(L)_2PbBr_4$–$(BA)_2(MA)_2Pb_3I_{10}$ (L = PEA, 2P or 2T) vertical heterostructures, respectively. Dashed lines are added in all the bright-field and PL images to ease the distinction between bromide (light blue) and iodide (yellow) domains. Scale bars, 5 µm. **s**,**t**, Comparisons of the halide interdiffusion coefficients in $(BA)_2PbBr_4$–$(BA)_2(MA)_{n-1}Pb_nI_{3n+1}$ ($n = 1$, 2, 3 or 5) and $(L)_2PbBr_4$–$(BA)_2(MA)_2Pb_3I_{10}$ (L = BA, PEA, 2P or 2T) vertical heterostructures, respectively, after heating at 80 °C. Left, Fickian diffusion coefficients; middle, non-Fickian diffusion coefficients calculated using the BM method; right, diffusion coefficients obtained using a KMC simulation. The boxes represent data points between 25 and 75 percentiles of the range, the whiskers represent the minimum-to-maximum range and the dashed lines highlight the average diffusion coefficients of the sample data points.

Note that for the $(BA)_2PbBr_4$–$(BA)_2PbI_4$ vertical heterostructure, no intermediate PL was observed after heating. In this case, the PL emission that originated from iodide diffusion into the bottom bromide perovskite was subsumed in the PL emission of the top $(BA)_2PbI_4$ layer, which is centred at ~521 nm at room temperature (Supplementary Fig. 7).

These observations are consistent with the conclusion that the green alloy PL emission originates from the bottom perovskite $(BA)_2PbBr_{4x}I_{4(1-x)}$ irrespective of the top perovskite ($(BA)_2(MA)_{n-1}Pb_nI_{3n+1}$; $n = 1$, 2, 3 or 5)). The diffusion coefficients for all three heterostructures are compared using the three diffusion models in Fig. 4s. The KMC predicted halide inter-diffusion coefficients are in the range of about 10^{-19} to 10^{-20} $m^2 s^{-1}$. All the models predicted that the halide interdiffusion increases with the inorganic layer thickness (n), which is consistent with the reported bromide–iodide interdiffusion coefficient of ~10^{-18} $m^2 s^{-1}$ for 3D perovskite heterostructure[14,16]. This observation suggests that a higher n facilitates a slightly faster halide migration. Therefore, for a given organic cation, 2D perovskites ($n = 1$) are better inhibitors of halide diffusion compared with quasi-2D ($n > 1$) and 3D perovskites. Overall, however, 2D perovskites with BA ligands do not show a substantially reduced anion diffusivity compared with those of 3D perovskites.

The effect of an organic cation on the halide interdiffusion in 2D perovskites was investigated by comparing BA with three larger cations—phenylethylammonium (PEA), biphenylethylammonium (2P) and bithiophenylethylammonium (2T)[18]. Figure 4 shows the schematic representations (Fig. 4j,m,p), bright-field

images (Fig. 4k,n,q) and PL images (Fig. 4l,o,r) of the $(PEA)_2PbBr_4$–$(BA)_2(MA)_2Pb_3I_{10}$, $(2P)_2PbBr_4$–$(BA)_2(MA)_2Pb_3I_{10}$ and $(2T)_2PbBr_4$–$(BA)_2(MA)_2Pb_3I_{10}$ vertical heterostructures, respectively. The heterostructures were heated at 80 °C and halide interdiffusion was tracked using PL (Supplementary Figs. 10–12). Similar to the previous cases, halide interdiffusion in $(PEA)_2PbBr_4$–$(BA)_2(MA)_2Pb_3I_{10}$ and $(2P)_2PbBr_4$–$(BA)_2(MA)_2Pb_3I_{10}$ vertical heterostructures led to the emergence of a single halide alloy PL peak centered at 507–511 nm (Supplementary Figs. 10 and 11). The calculated interdiffusion coefficients for several PEA- and 2P-based heterostructures using both analytical models and KMC simulations are shown in Fig. 4t.

Interestingly, for the $(2T)_2PbBr_4$–$(BA)_2(MA)_2Pb_3I_{10}$ vertical heterostructure, no obvious intermediate halide alloy emissions were observed even after 36 hours of heating at 80 °C (Supplementary Fig. 12), which indicates that there is a minimal amount of interdiffusion. After heating the heterostructure, we confirmed the absence of iodine in the bromide layer using SEM and EDS characterizations and excluded the possibility of a type II band alignment (resulting in PL quenching) through a detailed PL study on a series of bromide–iodide alloys for the 2T-based system (see Extended Data Fig. 5 for a detailed discussion). The quantification of the halide interdiffusion process for the 2T system was performed by assuming that the time for alloy formation (centred at ~510 nm) is longer than 36 hours and hence the model predicts an upper limit for the bromide–iodide interdiffusion coefficient. The 2T vertical heterostructures were not exposed to longer heating periods (>36 hours) due to defect formation, as evidenced by the development of lower energy PL emissions (Supplementary Fig. 12). The bromide–iodide interdiffusion coefficients for the $(2T)_2PbBr_4$–$(BA)_2(MA)_2Pb_3I_{10}$ vertical heterostructures using all three diffusion models are plotted in Fig. 4t. The interdiffusion coefficients for BA-, PEA-, 2P- and 2T-based vertical heterostructures using the KMC model are in the order of ~10^{-19}, ~10^{-20}, 10^{-20} and ~10^{-22} $m^2 s^{-1}$, respectively. All the diffusion models present a consistent trend, which indicates that bulkier π-conjugated organic cations, such as 2T, are much more efficient in inhibiting halide interdiffusion compared with benzene-based π-conjugated systems, such as 2P and PEA, or short-chain aliphatic organic cations, such as BA. Detailed information about the morphology, structural stability and diffusivity calculation parameters for all the heterostructures are given in Supplementary Figs. 13–16 and Supplementary Table 1.

Conclusions

We have demonstrated the assembly of atomically flat vertical heterostructures using two 2D halide perovskites. In contrast to classical solid-state interdiffusion models, which feature a continuous concentration profile evolution, a quantized layer-by-layer diffusion model governed by a concentration threshold and ion-blocking effects of the organic cations was discovered in 2D halide perovskites. Qualitative and quantitative halide interdiffusion analysis in $(BA)_2PbBr_4$–$(BA)_2(MA)_{n-1}Pb_nI_{3n+1}$ vertical heterostructures revealed that anionic migration is faster for a higher n number. Additionally, bulky and rigid thiophene-based conjugated organic cations were found to be much more effective stabilizers and inhibitors of halide interdiffusion compared with short aliphatic chains. These findings provide new insights about strategies to inhibit the intrinsic interdiffusion in halide perovskites and mitigate the instability of perovskite devices via molecular engineering. Moreover, the realization of vertical heterostructures also provides a materials platform for fundamental studies on the interplay between different 2D halide perovskites and their optoelectronic applications.

Online content

Any methods, additional references, Nature Research reporting summaries, source data, extended data, supplementary information, acknowledgements, peer review information; details of author contributions and competing interests; and statements of data and code availability are available at https://doi.org/10.1038/s41565-021-00848-w.

Received: 7 May 2020; Accepted: 7 January 2021;
Published online: 11 February 2021

References

1. Kojima, A., Teshima, K., Shirai, Y. & Miyasaka, T. Organometal halide perovskites as visible-light sensitizers for photovoltaic cells. *J. Am. Chem. Soc.* **131**, 6050–6051 (2009).
2. Burschka, J. et al. Sequential deposition as a route to high-performance perovskite-sensitized solar cells. *Nature* **499**, 316–319 (2013).
3. Zhou, H. et al. Interface engineering of highly efficient perovskite solar cells. *Science* **345**, 542–546 (2014).
4. Cao, Y. et al. Perovskite light-emitting diodes based on spontaneously formed submicrometre-scale structures. *Nature* **562**, 249–253 (2018).
5. Stranks, S. D. & Snaith, H. J. Metal–halide perovskites for photovoltaic and light-emitting devices. *Nat. Nanotechnol.* **10**, 391–402 (2015).
6. Zhu, H. et al. Lead halide perovskite nanowire lasers with low lasing thresholds and high quality factors. *Nat. Mater.* **14**, 636–642 (2015).
7. Saidaminov, M. I. et al. Planar-integrated single-crystalline perovskite photodetectors. *Nat. Commun.* **6**, 8724 (2015).
8. Snaith, H. J. et al. Anomalous hysteresis in perovskite solar cells. *J. Phys. Chem. Lett.* **5**, 1511–1515 (2014).
9. Vashishtha, P. & Halpert, J. E. Field-driven ion migration and color instability in red-emitting mixed halide perovskite nanocrystal light-emitting diodes. *Chem. Mater.* **29**, 5965–5973 (2017).
10. Yuan, Y. & Huang, J. Ion migration in organometal trihalide perovskite and its impact on photovoltaic efficiency and stability. *Acc. Chem. Res.* **49**, 286–293 (2016).
11. Xiao, Z. et al. Giant switchable photovoltaic effect in organometal trihalide perovskite devices. *Nat. Mater.* **14**, 193–198 (2015).
12. Eames, C. et al. Ionic transport in hybrid lead iodide perovskite solar cells. *Nat. Commun.* **6**, 7497 (2015).
13. Pan, D. et al. Visualization and studies of ion-diffusion kinetics in cesium lead bromide perovskite nanowires. *Nano Lett.* **18**, 1807–1813 (2018).
14. Zhang, Y. et al. Quantitative imaging of anion exchange kinetics in halide perovskites. *Proc. Natl Acad. Sci. USA* **116**, 12648–12653 (2019).
15. Lai, M. et al. Intrinsic anion diffusivity in lead halide perovskites is facilitated by a soft lattice. *Proc. Natl Acad. Sci. USA* **115**, 11929–11934 (2018).
16. Shewmon, N. T., Yu, H., Constantinou, I., Klump, E. & So, F. Formation of perovskite heterostructures by ion exchange. *ACS Appl. Mater. Interfaces* **8**, 33273–33279 (2016).
17. Saparov, B. & Mitzi, D. B. Organic–inorganic perovskites: structural versatility for functional materials design. *Chem. Rev.* **116**, 4558–4596 (2016).
18. Gao, Y. et al. Molecular engineering of organic–inorganic hybrid perovskites quantum wells. *Nat. Chem.* **11**, 1151–1157 (2019).
19. Lin, Y. et al. Suppressed ion migration in low-dimensional perovskites. *ACS Energy Lett.* **2**, 1571–1572 (2017).
20. Cao, D. H., Stoumpos, C. C., Farha, O. K., Hupp, J. T. & Kanatzidis, M. G. 2D homologous perovskites as light-absorbing materials for solar cell applications. *J. Am. Chem. Soc.* **137**, 7843–7850 (2015).
21. Smith, I. C., Hoke, E. T., Solis-Ibarra, D., McGehee, M. D. & Karunadasa, H. I. A layered hybrid perovskite solar cell absorber with enhanced moisture stability. *Angew. Chem. Int. Ed.* **53**, 11232–11235 (2014).
22. Saidaminov, M. I., Mohammed, O. F. & Bakr, O. M. Low-dimensional-networked metal halide perovskites: the next big thing. *ACS Energy Lett.* **2**, 889–896 (2017).
23. Dou, L. et al. Atomically thin two-dimensional organic–inorganic hybrid perovskites. *Science* **349**, 1518–1521 (2015).
24. Shi, E. et al. Two-dimensional halide perovskite lateral epitaxial heterostructures. *Nature* **580**, 614–620 (2020).
25. Wang, J. et al. Controllable synthesis of two-dimensional Ruddlesden–Popper-type perovskite heterostructures. *J. Phys. Chem. Lett.* **8**, 6211–6219 (2017).
26. Wang, J. X. et al. Controllable growth of centimeter-sized 2D perovskite heterostructures for highly narrow dual-band photodetectors. *ACS Nano* **13**, 5473–5484 (2019).
27. Hwang, B. H. & Lee, J.-S. 2D perovskite-based self-aligned lateral heterostructure photodetectors utilizing vapor deposition. *Adv. Opt. Mater.* **7**, 1801356 (2019).
28. Fu, Y. et al. Multicolor heterostructures of two-dimensional layered halide perovskites that show interlayer energy transfer. *J. Am. Chem. Soc.* **140**, 15675–15683 (2018).
29. Yuan, M. et al. Perovskite energy funnels for efficient light-emitting diodes. *Nat. Nanotechnol.* **11**, 872–877 (2016).

30. Wang, N. et al. Perovskite light-emitting diodes based on solution-processed self-organized multiple quantum wells. *Nat. Photon.* **10**, 699–704 (2016).
31. Xing, G. et al. Transcending the slow bimolecular recombination in lead–halide perovskites for electroluminescence. *Nat. Commun.* **8**, 14558 (2017).
32. Quan, L. N. et al. Tailoring the energy landscape in quasi-2D halide perovskites enables efficient green-light emission. *Nano Lett.* **17**, 3701–3709 (2017).
33. Shang, Q. et al. Unveiling structurally engineered carrier dynamics in hybrid quasi-two-dimensional perovskite thin films toward controllable emission. *J. Phys. Chem. Lett.* **8**, 4431–4438 (2017).
34. Slotcavage, D. J., Karunadasa, H. I. & McGehee, M. D. Light-induced phase segregation in halide–perovskite absorbers. *ACS Energy Lett.* **1**, 1199–1205 (2016).
35. Brivio, F., Caetano, C. & Walsh, A. Thermodynamic origin of photoinstability in the $CH_3NH_3Pb(I_{1-x}Br_x)_3$ hybrid halide perovskite alloy. *J. Phys. Chem. Lett.* **7**, 1083–1087 (2016).
36. Yin, W., Yan, Y. & Wei, S. Anomalous alloy properties in mixed halide perovskites. *J. Phys. Chem. Lett.* **5**, 3625–3631 (2014).
37. Fick, A. Ueber diffusion. *Ann. Phys.* **170**, 59–86 (1855).
38. Tuck, B. *Atomic Diffusion in III–V Semiconductors* Ch 2 (IOP, 1988).
39. Matano, C. On the relation between the diffusion-coefficients and concentrations of solid metals (the nickel–copper system). *Jpn J. Phys.* **8**, 109–113 (1993).
40. Arrhenius, S. A. Über die dissociationswärme und den einfluß der temperatur auf den dissociationsgrad der elektrolyte. *Z. Phys. Chem.* **4**, 96–116 (1889).
41. Arrhenius, S. A. Über die reaktionsgeschwindigkeit bei der Inversion von rohrzucker durch säuren. *Z. Phys. Chem.* **4**, 226–248 (1889).

Methods

Solvent evaporation method for the synthesis of a bottom bromide perovskite in a vertical heterostructure. For the synthesis of $(BA)_2PbBr_4$ nanocrystals, a concentrated precursor solution was prepared by dissolving 0.02 mmol *n*-butylammonium bromide (BA·HBr) and 0.01 mmol lead bromide ($PbBr_2$) in a 2 ml solution of dimethylformamide (DMF) and chlorobenzene (CB) (DMF:CB volume ratio of 1:1). The concentrated solution was diluted 60 times using a solvent system of CB, acetonitrile (AN) and dichlorobenzene (DCB) with a CB:AN:DCB volume ratio of 2.5:1:0.01. All the organic solvents (DMF, CB, AN and DCB) and $PbBr_2$ were purchased from Sigma Aldrich and used as received. BA·HBr was purchased from Greatcell Solar Ltd and used as received. Perovskite crystal synthesis using the solvent evaporation method was carried out in a glove box maintained under a nitrogen atmosphere. A sample vial that contained the silica/silicon dioxide (Si/SiO_2) substrate was then placed on a hot plate maintained at 50 °C. The Si/SiO_2 substrate was cleaned by dipping in a piranha solution for ~2 h to remove all trace impurities. The diluted precursor solution (10 µl) and AN (5 µl) were then dropped on the Si/SiO_2 substrate and the sample vial was capped for a slow evaporation of the solvents and subsequent growth of the perovskite crystals. The Si/SiO_2 substrate was removed from the hot plate once all the solvents were evaporated, which was typically within 15 min.

The syntheses of $(PEA)_2PbBr_4$, $(2P)_2PbBr_4$ and $(2T)_2PbBr_4$ nanocrystals followed the same procedure as detailed above for $(BA)_2PbBr_4$. For $(PEA)_2PbBr_4$, instead of BA·HBr, a phenylethylammonium bromide (PEA·HBr) precursor was used. For $(2P)_2PbBr_4$, instead of BA·HBr, a biphenylethylammonium bromide (2P·HBr) precursor was used. Similarly, a bithiophenylethylammonium bromide (2T·HBr) precursor was used for the synthesis of $(2T)_2PbBr_4$. The growth temperature used for the $(PEA)_2PbBr_4$ and $(2T)_2PbBr_4$ nanocrystals synthesis was 70 °C. PEA·HBr and $(2P)_2PbBr_4$ were purchased from Greatcell Solar Ltd and used as received. 2T·HBr salt was synthesized in our lab[18].

Slow cooling synthesis of bulk bromide perovskite crystals. $(BA)_2(MA)_2Pb_3Br_{10}$ bulk crystals were synthesized using a solution of 0.19 mmol BA·HBr, 0.40 mmol MA·HBr and 0.59 mmol lead oxide (PbO) in 0.9 ml of hydrogen bromic acid (HBr, 48 wt% in H_2O) and 0.1 ml of hypophosphorous acid (H_3PO_2, 50 wt% in H_2O). PbO, HBr and H_3PO_2 were purchased from Sigma Aldrich. MA·HBr was purchased from Greatcell Solar Ltd and used as received. The 10 ml solution vial was magnetically stirred and heated to 120 °C in an oil bath until the solution became transparent. The perovskite crystals formed after controlled cooling at a rate of ~5 °C h^{-1} are collected by vacuum filtration.

Slow cooling synthesis of bulk iodide perovskite crystals. For the synthesis of $(BA)_2PbI_4$ bulk crystals, a precursor solution was prepared by mixing 0.57 mmol *n*-butylammonium iodide (BA·HI) and 0.57 mmol PbO in 0.9 ml of hydroiodic acid (HI, 57 wt% in H_2O) and 0.1 ml of H_3PO_2 (50 wt% in H_2O). HI was purchased from Sigma Aldrich. BA·HI was purchased from Greatcell Solar Ltd. All the chemicals were used as received. The sample vial that contained the precursor solution was magnetically stirred and heated to 120 °C in an oil bath until all the salts completely dissolved. Once the solution was clear, the stirring was halted and the solution cooled down at a rate of ~5 °C h^{-1}. This controlled cooling process led to the nucleation and growth of perovskite crystals. The bulk crystals were extracted from the solution by vacuum filtration.

The synthesis of $(BA)_2(MA)Pb_2I_7$ bulk crystals was done by mixing 0.43 mmol BA·HI, 0.31 mmol methylammonium iodide (MA·HI) and 0.59 mmol PbO in an acid solution that contained 0.9 ml of HI (57 wt% in H_2O) and 0.1 ml of H_3PO_2 (50 wt% in H_2O). MA·HI was purchased from Greatcell Solar Ltd and used as received. The precursor solution in a 10 ml sample vial was magnetically stirred and heated to 120 °C in an oil bath until all the salts completely dissolved. The perovskite crystals were obtained by a controlled slow cooling at a rate of ~5 °C h^{-1} followed by vacuum filtration.

$(BA)_2(MA)_2Pb_3I_{10}$ bulk crystals were synthesized using a solution of 0.19 mmol BA·HI, 0.40 mmol MA·HI and 0.59 mmol PbO in 0.9 ml of HI (57 wt% in H_2O) and 0.1 ml of H_3PO_2 (50 wt% in H_2O). The 10 ml solution vial that contained the precursor solution was magnetically stirred and heated to 120 °C in an oil bath until the solution became transparent. The perovskite crystals were formed after controlled cooling at a rate of ~5 °C h^{-1} and collected by vacuum filtration.

Finally, the $(BA)_2(MA)_4Pb_5I_{16}$ bulk crystal synthesis involved a solution of 0.16 mmol BA·HI, 0.67 mmol MA·HI and 0.59 mmol PbO in 0.9 ml of HI (57 wt% in H_2O) and 0.1 ml of H_3PO_2 (50 wt% in H_2O). The 10 ml sample vial that contained the precursor solution was magnetically stirred and heated to 120 °C in an oil bath until all the precursor salts completely dissolved in the acid solution. The crystallized perovskites were formed and collected after controlled slow cooling at a rate of ~5 °C h^{-1} followed by vacuum filtration.

2D halide perovskite vertical heterostructure assembly. One or two pieces of iodide bulk crystals synthesized using the slow cooling method were transferred on the adhesive side of Scotch tape. A second Scotch tape was then stuck on the first tape and peeled off to exfoliate thinner layers of perovskite. This peeling-off process was repeated three to four times to ensure a very thin iodide layer with a good coverage over the entire adhesive tape. The Si/SiO_2 substrate with the bottom perovskite layer was then stuck on the Scotch tape that contained a thin exfoliated iodide perovskite layer. The Si/SiO_2 substrate with the Scotch tape was kept on a hot plate at 50 °C for ~3 min to ensure an efficient transfer of iodide perovskite from the tape to the substrate. The substrate was then removed from the hot plate, and the tape was finally peeled off, which resulted in the formation of a 2D bromide–iodide perovskite vertical heterostructure. The mechanical exfoliation process was carried out in a nitrogen-filled glove box.

Spin coating of polymethyl methacrylate on 2D perovskite vertical heterostructures. All 2D perovskite vertical heterostructures constructed in this study were encapsulated by spin coating a layer of ~30 µl of polymethyl methacrylate (PMMA) solution to protect against environmental degradation. PMMA 950K was purchased from Microchem and used for spin coating after further dilution with CB. The diluted PMMA solution was obtained by mixing a 3:1 volume ratio of PMMA 950K:CB. Spin coating was carried out at 1,500 r.p.m. for 1 min in a nitrogen-filled glove box. The spin-coated substrate was then heated on a hot plate at 50 °C for ~2 min to condense the PMMA and remove trace CB.

Spin coating of $(L)_2PbBr_{4x}I_{4(1-x)}$ 2D halide alloy thin films. The $(L)_2PbBr_4$ (L = BA or 2T) precursor solution was prepared by dissolving 0.05 mmol L·HBr (L = BA or 2T) and 0.05 mmol $PbBr_2$ in 0.6 ml of DMF. Similarly, the $(L)_2PbI_4$ (L = BA or 2T) precursor solution was prepared by dissolving 0.05 mmol L·HI (L = BA or 2T) and 0.05 mmol PbI_2 in 0.6 ml of DMF. Then, 100 µl of $(L)_2PbBr_{4x}I_{4(1-x)}$ (L = BA or 2T) solutions were prepared by mixing the $(L)_2PbBr_4$ and $(L)_2PbI_4$ (L = BA or 2T) precursor solutions in the desired stoichiometric ratios. For instance, $(L)_2PbBr_{1.6}I_{2.4}$ ($x = 0.4$) solution was prepared by mixing 40 µl of the $(L)_2PbBr_4$ solution with 60 µl of the $(L)_2PbI_4$ solution. Then, 30 µl of the prepared $(L)_2PbBr_{4x}I_{4(1-x)}$ solution was spin coated on an Si/SiO_2 substrate. Spin coating was carried out at 1,500 r.p.m. for 1 min in a nitrogen-filled glove box. The spin-coated thin films were used for PL characterization of the $(L)_2PbBr_{4x}I_{4(1-x)}$ 2D halide alloys. The experimentally obtained PL energy versus bromide mole fraction correlation for $(BA)_2PbBr_{4x}I_{4(1-x)}$ was then used as the calibration to calculate the alloy compositions for all the heterostructures presented in this work.

Characterizations. *Bright-field imaging.* All bright-field images were collected with a custom Olympus BX53 microscope.

PL imaging and PL spectrum. All PL images were captured using a X-Cite Series 120 Q lamp as the excitation source. A coherent OBIS 375 nm laser excitation source was used for all the PL spectrum measurements. The filter cube in an Olympus BX53 microscope contains a bandpass filter (330–385 nm) for excitation and a dichroic mirror (cutoff wavelength, 400 nm) for light splitting. PL spectra were collected with a SpectraPro HRS-300 spectrometer.

Confocal imaging. A Leica SP8 inverted laser scanning confocal microscope with a 405 nm laser line as the excitation wavelength was used for the PL mapping of the bromide and iodide layers in the vertical heterostructure.

AFM imaging. AFM images were recorded in the tapping mode using a Veeco multimode atomic force microscope.

SEM imaging and EDS mapping. SEM images were captured using a Quanta 650 FEG SEM at 10 kV and 4.5 spot size with an Everhart–Thornley detector. EDS spectra and elemental mappings were collected using an EDAX Element Silicon Drift Detector at the same beam conditions as for the SEM images.

Cross-sectional STEM imaging and EDS mapping. The cross-sectional samples were prepared by a multibeam focused ion beam system (JEOL JIB-4700F). To minimize ion-beam-induced damage, the whole focused ion beam polishing process was carried out at a reduced voltage and ion-beam current. The 2 µm thick sample was extracted with an accelerating voltage of 30 kV and a reduced ion beam of less than 1 nA. After the lamella were transferred to the transmission electron microscopy grid, it was gradually thinned to approximately 500 nm with an ion beam of accelerating voltage of 10 kV and gradually reducing current of 100 pA and 30 pA. After that, the voltage was reduced further to 5 kV and a current as small as 10 pA was used for the final milling. STEM images and EDS elemental maps were carried out on a JEOL JEM-F200 microscope at 200 kV.

XRD. The XRD of vertical heterostructures and pure perovskites was measured with a Rigaku Smart Lab using a Cu Kα source ($\lambda = 1.54056$ Å) in the Bragg Brentano mode.

Simulations. *DFT calculations.* The Vienna ab initio Simulation Package version 5.4 was used to perform the DFT calculations for geometry optimization and predicting the electronic properties[42,43]. The projector augmented wave potentials were applied, with 1*s* of H, 2*s*2*p* of C and N, 4*s*4*p* of Br, 5*s*5*p* of I and 5*d*6*s*6*p* of Pb as valence electrons[44,45]. The generalized gradient approximation of Perdew, Burke and Ernzerhof was employed. The energy cutoff for the plane-wave basis set was set as 500 eV (ref. [46]). A Γ-centred 3 × 3 × 1 k-points mesh was used for the structural

relaxation and a 6×6×1 mesh for the projected density of state calculations. Under the applied settings, the total energy was converged to ≤1 meV atom^{-1} with respect to a higher kinetic energy cutoff or denser k-point mesh. The convergence threshold for structural optimization was set at 0.025 eV Å^{-1}. A D3 correction method with Becke–Jonson damping was applied to account for the van der Waals interaction[47]. The projected density of state calculations were performed with spin–orbital coupling corrections switched on[48]. Two materials—BA_2PbBr_4 ($n=1$) and $BA_2MA_2Pb_3I_{10}$ ($n=3$)—were investigated. To allow for concentration variation in the halide species, 2×2×2 unit cells were used. To model the hybrid perovskite samples in different diffusion stages, different ratios of Br atoms to I atoms were substituted in BA_2PbBr_4 ($n=1$) and I atoms to Br atoms were substituted in $BA_2MA_2Pb_3I_{10}$ ($n=3$).

KMC simulations. The KMC simulations consist of a 2D lattice of sites that correspond to Pb octahedra, which were identified as containing either I or Br ions[49,50]. The number of columns of simulation was arbitrarily chosen to have 100 sites for the ease of implementation, and the number of rows reflected the number of repeat octahedron layers inside each system (such that the total height comprised the total number of perovskite sheets). Partial periodic boundary conditions were implemented, which permitted periodicity only between the first and last columns of a row. The ions can move from one site to a neighbouring site by a hopping event, the rate of which is controlled by a transition rate, k. There are two types of hopping events: an exchange between an identical pair of ions and an exchange between a dissimilar pair of ions. We were interested in fitting only in the latter case (that is, the hopping event that results in a change of occupancy), as this propagates the system to a different state that can be observed. The former case was ignored and is not available as a hopping event.

A standard KMC algorithm was used and a hopping event occurred at every KMC step. There were four possible moves for a given site, each with a transition probability of k, and a list was formed that contained all the possible moves and associated k. The total rate coefficient, $k_{\text{total}} = \sum_{i=1}^{M} k_i$, with M being the total number of possible moves, was calculated, along with a list (R) that contained the cumulative rates $R_i = \sum_{j=1}^{i} k_i$, for $i = 1, \ldots, M$. The transition that satisfied $R_{i-1} < uR \leq R_i$, where $u \in (0,1)$ is a uniform random deviate, was chosen and the hopping event carried out. The rates were recalculated, and the elapsed system time incremented with a variable time step (Δt), which was randomly chosen from a Poisson distribution:

$$\Delta t = -\ln(u) k_{\text{total}}^{-1}$$

where $u \in (0,1)$ and is independent of the u chosen for the hopping event.

To capture the experimental behaviour of the Br layer to equilibrate to its preferred alloy composition, a concentration threshold constraint was implemented, such that once the concentration of the Br species in a given layer reached its preferred concentration, diffusion from the layer was suppressed (by setting $k=0$). An additional constraint was implemented in the case of $(BA)_2PbBr_4$–$(BA)_2PbI_4$ to capture the observed population inversion. To avoid reaching a steady-state concentration of 50:50, the backwards diffusion of a Br ion to its originating layer was suppressed (with $k=0$). The transition rates, k, were fit so that the elapsed simulation time required for the bottom perovskite Br layer to reach its thermodynamically preferred alloy composition, as determined experimentally, reproduced the experimental time. Once the transition rates were determined, the diffusion coefficients were calculated by $D = k h_{\text{Br}}^2$ where h_{Br} is the experimentally measured bromide layer thickness.

Data availability

All the data are available in the article or its Supplementary Information. All the materials are available upon request to L.D.

References

42. Kresse, G. Ab initio molecular dynamics for liquid metals. *J. Non-Cryst. Solids* **192-193**, 222–229 (1995).
43. Kresse, G. & Furthmüller, J. Efficient iterative schemes for ab initio total-energy calculations using a plane-wave basis set. *Phys. Rev. B* **54**, 11169–11186 (1996).
44. Blöchl, P. E. Projector augmented-wave method. *Phys. Rev. B* **50**, 17953–17979 (1994).
45. Kresse, G. & Furthmüller, J. Efficiency of ab-initio total energy calculations for metals and semiconductors using a plane-wave basis set. *Comput. Mater. Sci.* **6**, 15–50 (1996).
46. Kresse, G. & Hafner, G. Ab initio molecular-dynamics simulation of the liquid–metal-amorphous–semiconductor transition in germanium. *Phys. Rev. B* **49**, 14251–14269 (1994).
47. Grimme, S., Antony, J., Ehrlich, S. & Krieg, H. A consistent and accurate ab initio parametrization of density functional dispersion correction (DFT-D) for the 94 elements H–Pu. *J. Chem. Phys.* **132**, 154104 (2010).
48. Steiner, S., Khmelevskyi, S., Marsmann, M. & Kresse, G. Calculation of the magnetic anisotropy with projected-augmented-wave methodology and the case study of disordered $Fe_{1-x}Co_x$ alloys. *Phys. Rev. B* **93**, 224425 (2016).
49. Stoltze, P. *Simulation Methods in Atomic Scale Materials Physics* (Polyteknisk, 1977).
50. Fichthorn, K. A. & Weinberg, W. H. Theoretical foundations of dynamical Monte Carlo simulations. *J. Chem. Phys.* **95**, 1090–1096 (1991).

Acknowledgements

This work is supported by the Office of Naval Research (Grant no N00014-19-1-2296, Program Managers, J. Parker and P. Armistead). Akriti acknowledges support from the Frederick N. Andrews Fellowship. B.P.F. acknowledges support from the Purdue Process Safety & Assurance Center. B.M.S. acknowledges the Air Force Office of Scientific Research (AFOSR) for their support (Grant no. FA9550-18-S-0003, Program Manager, K. Caster). The DFT computational work by P.L. and J.Y. is supported in part through computational resources provided by the Information Technology Department at Purdue University. The transmission electron microscopy work is supported by funding from the National Natural Science Foundation of China (Grant no. 21805184), the Natural Science Foundation of Shanghai (Grant no. 18ZR1425200) and the Center for High-Resolution Electron Microscopy (ChEM) at ShanghaiTech University (Grant no. EM02161943). We thank Q. Zhao, L. Huang, R. Agrawal, B. W. Boudouris and C. Davis for helpful discussions.

Author contributions

Akriti and E.S. synthesized and characterized the 2D perovskite vertical heterostructures; Akriti performed the analytical calculations of the halide interdiffusion coefficients; S.B.S. and B.M.S. performed the KMC simulations and data analysis; J.Y. and P.L. carried out the DFT calculations; C.L.A.-M. and A.J.P. participated in the heterostructure fabrication and optical characterization; B.Y., X.H. and Y.Y. conducted the STEM characterization; Y.G. performed the organic ligand synthesis; B.P.F. performed the SEM and EDS characterizations; Akriti and L.D. wrote the manuscript; all the authors read and revised the manuscript. L.D. supervised the project.

Competing interests

Authors declare no competing interests.

Additional information

Extended data is available for this paper at https://doi.org/10.1038/s41565-021-00848-w.

Supplementary information The online version contains supplementary material available at https://doi.org/10.1038/s41565-021-00848-w.

Correspondence and requests for materials should be addressed to L.D.

Peer review information *Nature Nanotechnology* thanks Dehui Li, Biwu Ma and the other, anonymous, reviewer(s) for their contribution to the peer review of this work.

Reprints and permissions information is available at www.nature.com/reprints.

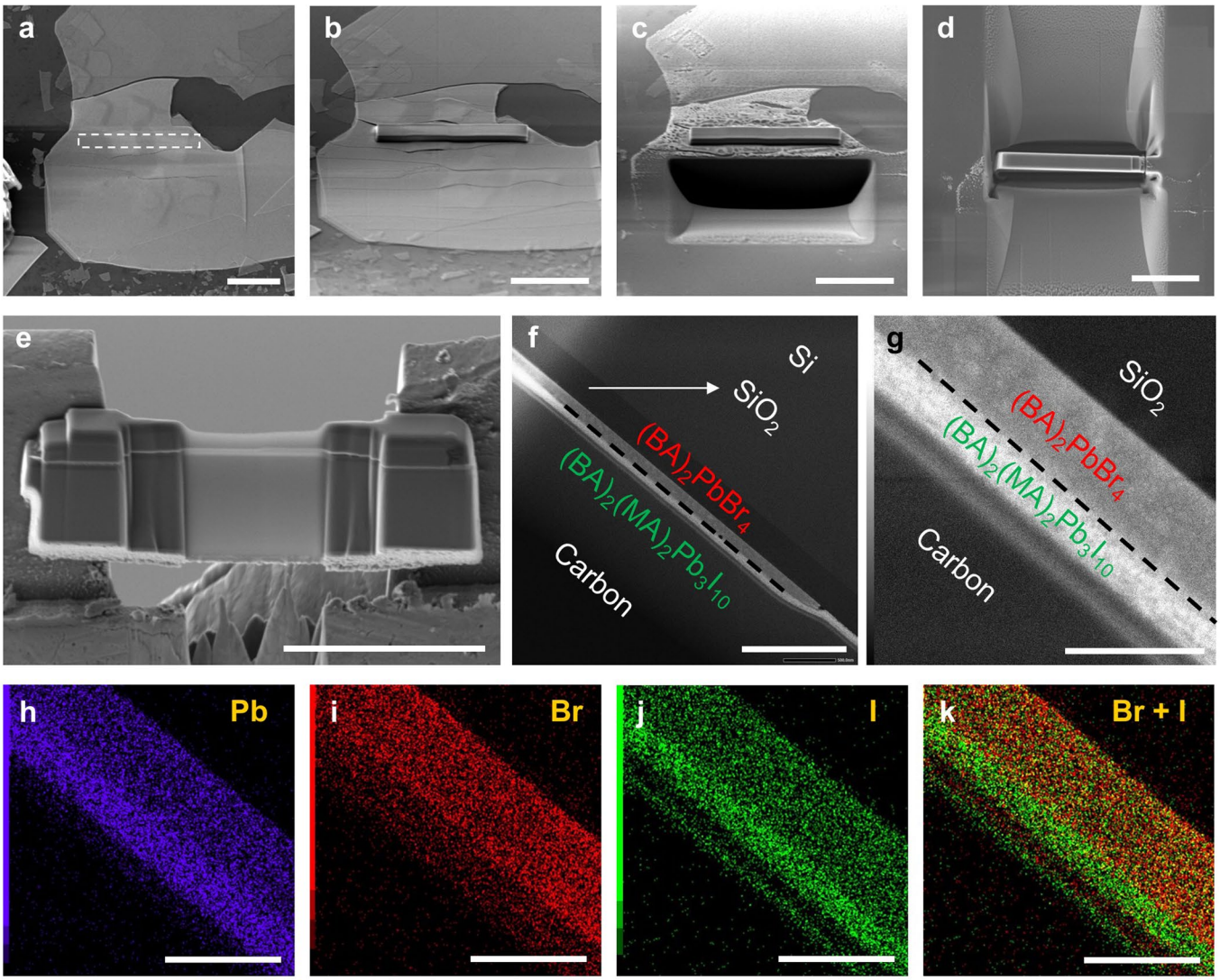

Extended Data Fig. 1 | Cross-sectional characterization of $(BA)_2PbBr_4$-$(BA)_2(MA)_2Pb_3I_{10}$ vertical heterostructure. a, SEM image of the vertical heterostructure (top view). The dashed rectangle highlights the area used for cross-sectional characterization. **b**, Carbon coating of the rectangular area of interest. Preparation of the cross-sectional lamella by **c**, digging a hole and **d**, thinning by Ga ions. **e**, Prepared cross-section of the vertical heterostructure. Scale bars in **a**–**e** are 10 µm. **f**, Low-magnification STEM image of the vertical heterostructure. The scale bar is 1 µm. **g**, Enlarged STEM image of the vertical heterostructure. STEM images show a clear interface between $(BA)_2PbBr_4$ and $(BA)_2(MA)_2Pb_3I_{10}$. EDS elemental mapping of **h**, Pb, **i**, Br, and **j**, I. **k**, Overlaid bromine and iodine EDS mapping. Scale bars in **g**–**k** are 200 nm. The brighter bromine and iodine signals in the EDS elemental mappings are mainly concentrated in the pure phase $(BA)_2PbBr_4$ and $(BA)_2(MA)_2Pb_3I_{10}$ regions, respectively. The dimmer Br signal from $(BA)_2(MA)_2Pb_3I_{10}$ region and iodine signal from $(BA)_2PbBr_4$ region can be attributed to diffusion, which is likely caused by the harsh sputtering and focused ion-beam milling during the cross-sectional sample preparation. These results suggest that electron microscopy is not an ideal tool to study the anion inter-diffusion kinetics for 2D halide perovskites due to sample damage.

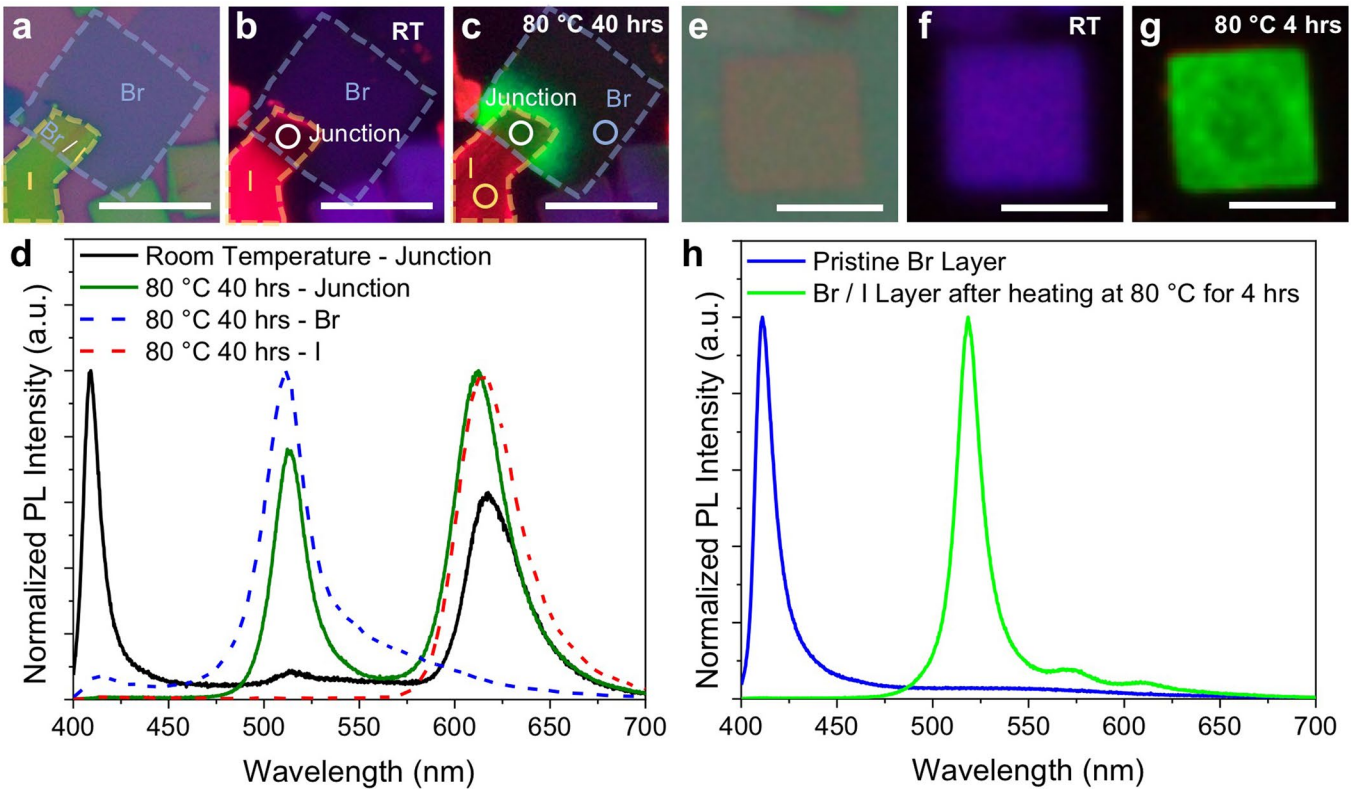

Extended Data Fig. 2 | Analysis of origin of halide alloy PL peak in $(BA)_2PbBr_4$-$(BA)_2(MA)_2Pb_3I_{10}$ vertical heterostructure after heating at 80 °C. **a**, Bright-field image of vertical heterostructure. **b, c**, PL image of vertical heterostructure at room temperature and after heating at 80 °C for 40 hrs, respectively. The circled regions denote the area used for PL emission measurement of the heterostructure, bromide perovskite and iodide perovskite. Dashed lines are added in all the bright-field and PL images for the ease of distinction of bromide (light blue) and iodide (yellow) domains. Scale bars in **a**–**c** are 10 μm. **d**, PL spectrum of the vertical heterostructure before and after heating at 80 °C for 40 hrs. Presence of halide alloy PL peak at ~ 511 nm (dashed blue curve) is evident in bromide perovskite layer. No new PL peak (dashed red curve) is observed in iodide perovskite layer after the heating process. **e, f**, Bright-field and PL image of $(BA)_2PbBr_4$, respectively. **g**, PL image of the $(BA)_2PbBr_{4x}I_{4(1-x)}$ alloy formed after placing bulk crystal of $(BA)_2(MA)_2Pb_3I_{10}$ on top of $(BA)_2PbBr_4$ nanocrystal and heating it for 4 hrs at 80 °C. The bulk crystal of $(BA)_2(MA)_2Pb_3I_{10}$ is removed after the heating process to analyze the formation of $(BA)_2PbBr_{4x}I_{4(1-x)}$ perovskite in the bottom layer. Scale bars in **e**–**g** are 5 μm. **h**, PL spectrum of $(BA)_2PbBr_4$ nanocrystal at room temperature and $(BA)_2PbBr_{4x}I_{4(1-x)}$ alloy formed in the bottom layer after heating $(BA)_2PbBr_4$-$(BA)_2(MA)_2Pb_3I_{10}$ vertical heterostructure at 80 °C for 4 hrs.

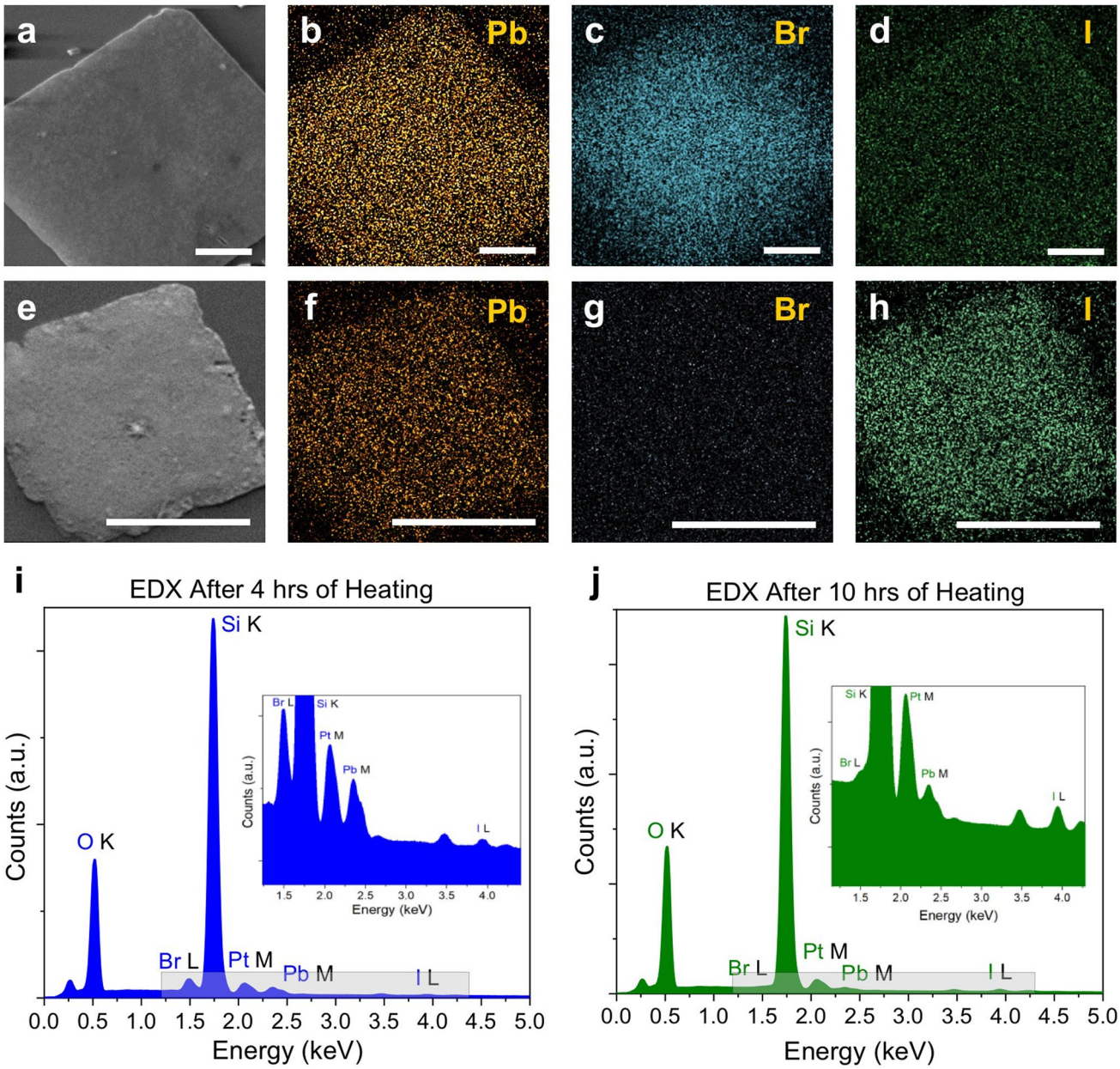

Extended Data Fig. 3 | SEM / EDS imaging of $(BA)_2PbBr_4$-$(BA)_2(MA)_2Pb_3I_{10}$ vertical heterostructure. SEM images of $(BA)_2PbBr_{4x}I_{4(1-x)}$ alloy formed after placing bulk crystal of $(BA)_2(MA)_2Pb_3I_{10}$ on top of $(BA)_2PbBr_4$ nanocrystal and heating it for **a**, 4 hrs and **e**, 10 hrs at 80 °C. EDS elemental mappings of **b, f**, Pb, **c, g**, Br, and **d, h**, I for the SEM images in **a** and **e**, respectively. All scale bars are 3 µm. **i, j**, EDS spectrum corresponding to the SEM images in **a** and **e**, respectively. The insets show the zoomed-in spectrum to highlight the bromine and iodine counts. The weak iodine signal in EDS elemental mapping and spectrum after 4 hrs of heating suggest that the iodine ions diffused to only top few layers of the bromide perovskite after 4 hrs of heating. After 10 hrs of heating, almost all the bromide perovskite layers show dominant iodine composition as evident from the EDS mapping and spectrum.

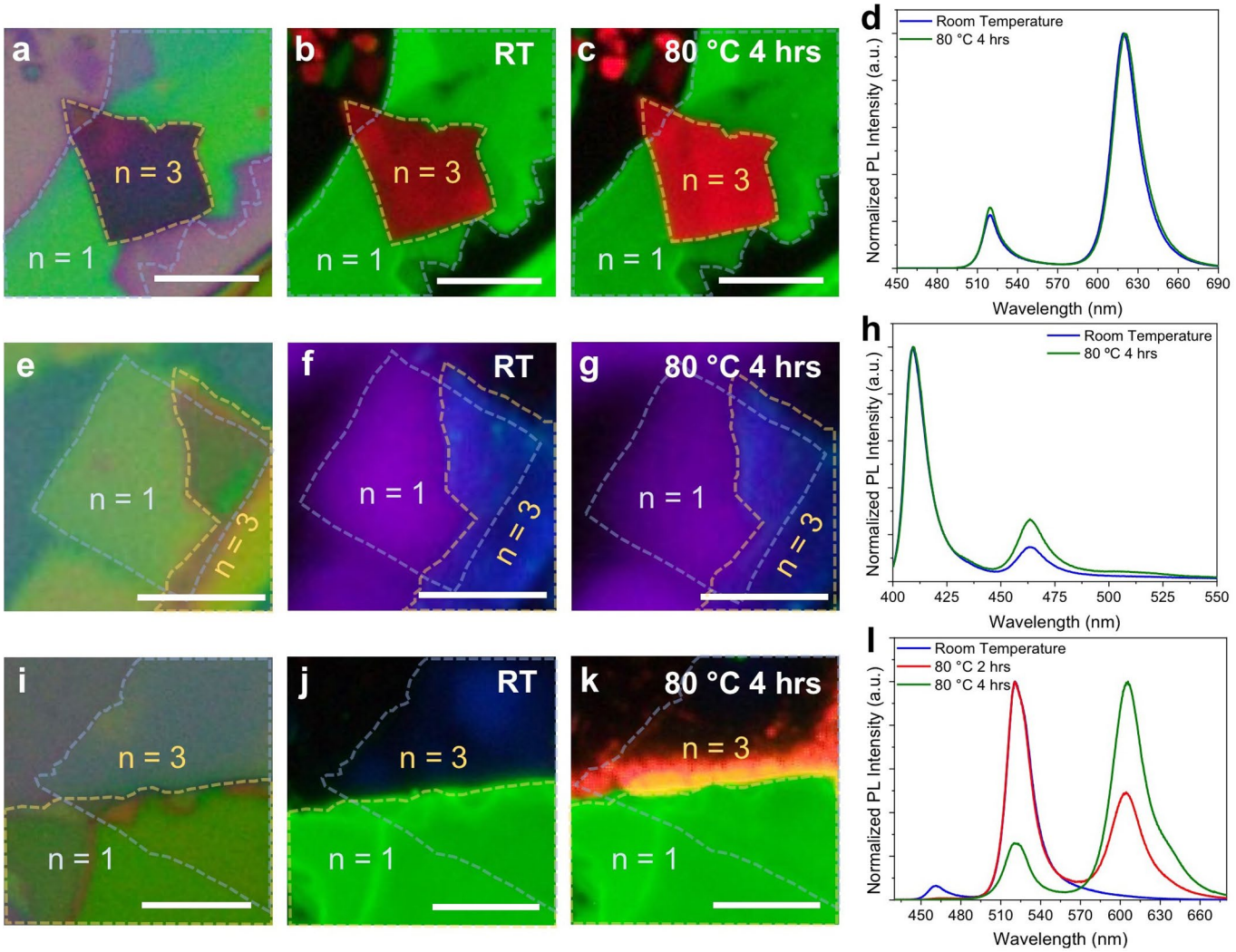

Extended Data Fig. 4 | Analysis of new phase formation in $(BA)_2PbX_4$-$(BA)_2(MA)_2Pb_3X_{10}$ (X = I, Br) and alloy formation in $(BA)_2(MA)_2Pb_3Br_{10}$-$(BA)_2PbI_4$ vertical heterostructures after heating at 80 °C. a, Bright-field image of $(BA)_2PbI_4$-$(BA)_2(MA)_2Pb_3I_{10}$ vertical heterostructure. **b, c**, PL images of $(BA)_2PbI_4$-$(BA)_2(MA)_2Pb_3I_{10}$ vertical heterostructure at room temperature and after heating at 80 °C for 4 hrs, respectively. **d**, PL spectrum of $(BA)_2PbI_4$-$(BA)_2(MA)_2Pb_3I_{10}$ vertical heterostructure before and after heating at 80 °C for 4 hrs. No PL shift and no new PL emission from any new halide perovskite phases is observed after the heating process. **e**, Bright-field image of $(BA)_2PbBr_4$-$(BA)_2(MA)_2Pb_3Br_{10}$ vertical heterostructure. **f, g**, PL images of $(BA)_2PbBr_4$-$(BA)_2(MA)_2Pb_3Br_{10}$ vertical heterostructure at room temperature and after heating at 80 °C for 4 hrs, respectively. **h**, PL spectrum of $(BA)_2PbBr_4$-$(BA)_2(MA)_2Pb_3Br_{10}$ vertical heterostructure before and after heating at 80 °C for 4 hrs. No PL shift and no new PL emission from any new halide perovskite phases is observed after the heating process. **i**, Bright-field image of $(BA)_2(MA)_2Pb_3Br_{10}$-$(BA)_2PbI_4$ vertical heterostructure. **j, k**, PL images of $(BA)_2(MA)_2Pb_3Br_{10}$-$(BA)_2PbI_4$ vertical heterostructure at room temperature and after heating at 80 °C for 4 hrs, respectively. **l**, PL spectrum of $(BA)_2(MA)_2Pb_3Br_{10}$-$(BA)_2PbI_4$ vertical heterostructure before and after heating at 80 °C. Alloy peak centered ~ 605 nm observed after heating indicates formation of iodide dominant $(BA)_2(MA)_2Pb_3Br_{10x}I_{10(1-x)}$ (n = 3) alloy perovskite rather than $(BA)_2PbBr_{4x}I_{4(1-x)}$ (n = 1) alloy perovskite. Dashed lines are added in all the bright-field and PL images for the ease of distinction of bottom (light blue) and top (yellow) perovskite domains. All scale bars are 5 μm.

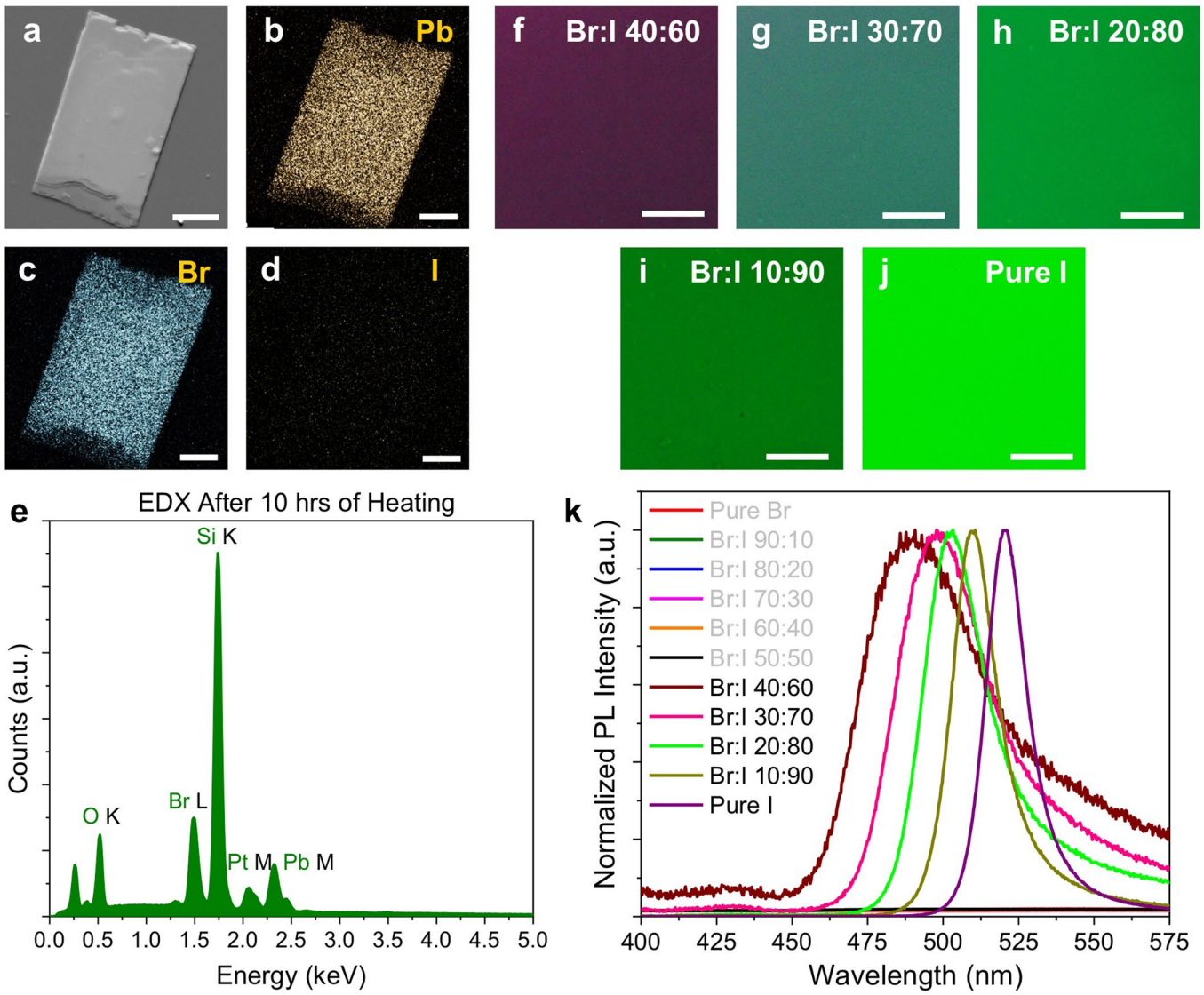

Extended Data Fig. 5 | Investigation of halide inter-diffusion in $(2T)_2PbBr_4$-$(BA)_2(MA)_2Pb_3I_{10}$ vertical heterostructure. a, SEM image of bottom bromide perovskite layer after placing bulk crystal of $(BA)_2(MA)_2Pb_3I_{10}$ on top of $(2T)_2PbBr_4$ nanocrystal and heating it for 10 hrs at 80 °C. **b, c, d**, EDS elemental mappings of Pb, Br, and I, respectively, for the SEM image in **a**. Scale bars in **a**–**d** are 10 μm. **e**, EDS spectrum corresponding to the SEM image in **a**. **f, g, h, i, j**, PL images of thin films of $(2T)_2PbBr_{4x}I_{4(1-x)}$ alloy perovskite with $x_{Br} = 0.4$, 0.3, 0.2, 0.1, and 0, respectively. All scale bars are 20 μm. **k**, PL emission spectrum of alloy perovskites with $x_{Br} = 1$,0.9, 0.8, 0.7, 0.6, 0.5, 0.4, 0.3, 0.2, 0.1, and 0. The legend texts for $x_{Br} > 0.4$ have been shown in grey color to highlight that no PL is observed for these compositions. Note that $(2T)_2PbBr_4$ perovskite has no PL emission due to type II band alignment between the inorganic $[PbBr_4]^{2-}$ and organic ligand $2T^+$ layers. The red PL emission in $(2T)_2PbBr_4$-$(BA)_2(MA)_2Pb_3I_{10}$ vertical heterostructure comes from the top iodide perovskite layer. However, $(2T)_2PbI_4$ has type I band alignment with green PL emission. As all other heterostructures show an alloy PL emission peak which is iodide dominant, we expected the halide inter-diffusion in 2T system to be thermodynamically driven towards formation of an iodine dominated $(2T)_2PbBr_{4x}I_{4(1-x)}$ perovskite with green PL emission. To ensure that absence of green alloy PL emission in 2T system indicates absence of iodide diffusion rather than quenched PL of iodide dominant alloy perovskite, it is important to estimate the bromide concentration at which the $(2T)_2PbBr_{4x}I_{4(1-x)}$ alloy perovskite transitions from type II to type I band alignment. Extended Data Fig. 5f–k shows the PL emission spectrum of $(2T)_2PbBr_{4x}I_{4(1-x)}$ alloy perovskites obtained by spin coating the bromide and iodide precursor solutions mixed in the desired stoichiometric ratios. It is evident from Extended Data Fig. 5k that for $x_{Br} \leq 0.4$, $(2T)_2PbBr_{4x}I_{4(1-x)}$ perovskite has type I band alignment and for $x_{Br} > 0.4$, it transitions to type II band alignment. Therefore, the absence of alloy PL emission in the diffusion studies is indicative of the inhibiting role of 2T organic cation rather than type II band alignment of iodide dominant alloy perovskites.